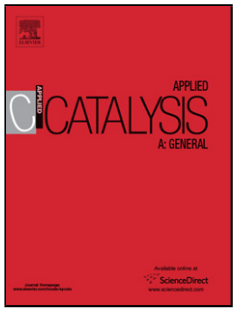

Title: Effect of γ-Alumina Nanorods on CO Hydrogenation to Higher Alcohols over Lithium-Promoted CuZn-based Catalysts

Authors: SuMin Choi, YoungJong Kang, SangWoo Kim

PII: S0926-860X(17)30479-9
DOI: https://doi.org/10.1016/j.apcata.2017.10.001
Reference: APCATA 16432

To appear in: *Applied Catalysis A: General*

Received date: 29-6-2017
Revised date: 21-9-2017
Accepted date: 4-10-2017

Please cite this article as: SuMin Choi, YoungJong Kang, SangWoo Kim, Effect of γ-Alumina Nanorods on CO Hydrogenation to Higher Alcohols over Lithium-Promoted CuZn-based Catalysts, Applied Catalysis A, General https://doi.org/10.1016/j.apcata.2017.10.001

Effect of γ-Alumina Nanorods on CO Hydrogenation to Higher Alcohols over Lithium-Promoted CuZn-based Catalysts

SuMin Choi[1,2], YoungJong Kang[2], SangWoo Kim[1,3,*]

[1]*Clean Energy Research Center, Korea Institute of Science and Technology, Hwarangno 14-gil 5, Sungbuk-Gu, Seoul 02792, Republic of Korea*

[2]*Department of Chemistry, Hanyang University, 222 Wangsimni-ro, Seongdong-gu, Seoul, Republic of Korea*

[3]*Division of Energy & Environment Technology, KIST school, University of Science and Technology (UST), Seoul 02792, Republic of Korea.*

* Corresponding author.

*E-mail *swkim@kist.re.kr*

Tel: +82-958-5526

Graphical abstract

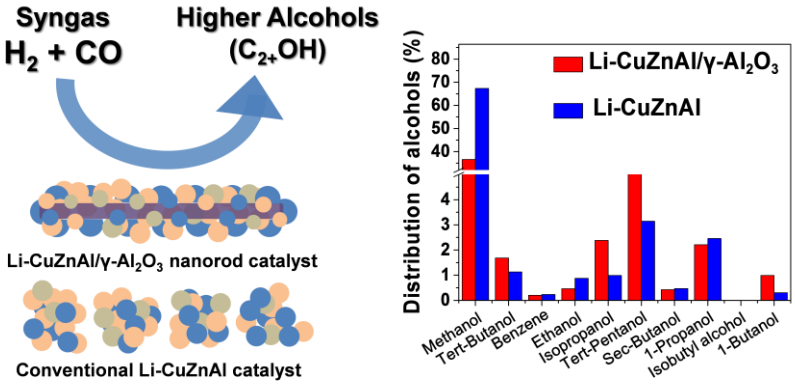

Highlights

- The introduction of γ-Al_2O_3 nanorods and Al^{3+} ions to a Li-promoted Cu-Zn-based catalyst promotes CO hydrogenation to higher alcohols.
- The enhanced catalytic performance of the catalyst is due to the reduction in CuO crystallite size, incurred by the thermal degradation of hydrotalcite precursors, and due to the increase in basicity.
- In particular, a Li-$Cu_{0.45}Zn_{0.45}Al_{0.1}$ catalyst supported on γ-Al_2O_3 nanorods is the most optimized for the synthesis of 2-methyl branched alcohols among the higher alcohol products.
- The modified catalyst exhibits excellent thermal stability over long-term reactions due to the sintering resistance of nanorods and a refractory $CuAl_2O_4$.

ABSTRACT

To achieve high catalytic activities and long-term stability to produce higher alcohols via CO hydrogenation, the catalytic activities were tuned by controlling the loading amounts of γ-alumina nanorods and Al^{3+} ions added to modify Cu-Zn catalysts promoted with Li. The selectivity of higher alcohols and the CO conversion to higher alcohols over a Li-modified $Cu_{0.45}Zn_{0.45}Al_{0.1}$ catalyst supported on 10% nanorods were 1.8 and 2.7 times higher than those with a Cu-Zn catalyst without nanorods and Al^{3+} ions, respectively. The introduction of the thermally and chemically stable γ-Al_2O_3 nanorod support and of Al^{3+} to the modified catalysts improves the catalytic

activities by decreasing the crystalline size of CuO and increasing the total basicity. Along with the nanorods, a refractory $CuAl_2O_4$ formed by the thermal reaction of CuO and Al^{3+} enhances the long-term stability by increasing the resistance to sintering of the catalyst.

Keywords: Cu-Zn-Al Catalyst, Alumina nanorods, CO hydrogenation, Higher alcohols, Li-Promoter, Syngas.

1. Introduction

Global warming and environmental pollution have led researchers to devote much attention to the synthesis of higher alcohols. To mitigate the strong dependence on natural oil, alternative fuels such as coal, natural gas, biomass, and shale gas have attracted enormous interest [2,3]. Higher alcohols ($C_{2+}OH$), which are converted to carbon-based feedstocks (biomass, coal, natural gas) [3–5], have been used as alternative fuels and chemical feedstocks [6–10]. To synthesize higher alcohols, many researchers have experimented using different types of catalysts, which are classified as Rh-based catalysts [9,11,12], Mo-based catalysts [9,13,14], and Cu-based catalysts such as modified Fischer-Tropsch (FT) catalysts [9,15] and alkali-promoted methanol catalysts [9,16–18].

Catalysts containing Rh have a high selectivity to synthesize higher alcohols using syngas, but they are too expensive for industrial application [11,19]. Mo-based catalysts (MoS_2, Mo_2C) [20,21] are resistant to sulfur and less sensitive to CO_2, but the catalytic process requires high pressure and high temperature; they also require a long reaction time to reach a stable state [14].

Cu-based catalysts are relatively inexpensive compared to Rh- or Mo-based catalysts and are of interest because of their ability to synthesize higher alcohols by a simple method that involves doping alkali into the Cu-based catalysts [16,17]. Modified FT catalysts (Cu-Co, Cu-Fe, and Cu-Ni) are promising with respect to higher alcohol synthesis using syngas [22,23]. However, since the Cu-Co catalyst has a low catalytic stability in long-term operation and a low total alcohol selectivity, it is unsuitable for use in industrial processes [15,24]. The Cu-Fe catalyst has a phase change between Cu and Fe, which weakens or interrupts the interaction between the two

transition metals, which adversely affects the CO hydrogenation reaction [25]. The Cu-Ni catalyst is more suitable for methanol synthesis than higher alcohol synthesis due to the formation of the binary metal alloy [26]. All the modified FT catalysts are inappropriate because hydrocarbons are produced in large amounts, which decrease the content of higher alcohols during FT reactions.

Cu-Zn-based methanol catalysts promoted with alkali metals have been widely used because they are highly effective in the synthesis of higher alcohols due to their high activity in mild environments. However, since the catalysts tend to be sintered at high temperature and high pressure, the catalytic activities tend to drop sharply [16,17]. Thus, to prevent deactivation from sintering of the catalysts, metal additives such as Al, Cr, Ce, and Mn are added to the Cu-Zn catalysts [16,26,27]. Addition of these metals to the catalysts increases the specific surface area to prevent aggregation, allowing the activity and selectivity of the catalyst to be improved. Cu-Zn-Cr and Cu-Zn-Ce catalysts operate at high pressure (up to 7.6 and 20 MPa, respectively) to synthesize alcohols [16,27]. Cu-Zn-Mn shows an increase in the production of methanol and higher alcohol selectivity with lower overall activity [26]. Cu-Zn-Al catalysts, which can be used under milder conditions, show an optimum catalytic performance in the synthesis of higher alcohols [26].

To increase the catalytic activity of Cu-based catalysts, it is important to choose an appropriate alkali promoter for higher conversion and selectivity. The role of the alkali enhancer is to neutralize the surface acidity of the catalyst and/or support and to facilitate the adsorption of CO molecules on the catalyst surface [28]. However, if too much enhancer is used, the active sites are blocked, which lowers the catalytic activity [29]. In general, the alkali promoters used are mainly Na, K, Rb, Cs, and Li in Cu-based catalysts [30]. K mainly increases the selectivity to methanol and ethanol [23], and Na has the highest selectivity of higher alcohol at the beginning only because of its low stability [23]. Cs predominantly produces methanol [23]. Cu-based catalysts promoted with Li have lower activity than those with other promoters but have increased selectivity for higher alcohols around 300°C and are more stable during the reaction [23,31].

On the other hand, the catalytic activity and selectivity for higher alcohols are not solely dependent on the addition of alkaline ions but also depend on the counter anions of the salt and the support. The counter anion of the alkali salt chosen for alcohol selectivity should be easily removed by the alkali, and the alkali salt should be evenly distributed over the catalyst. For even dispersion of the catalyst, the alkali promoter with a relatively low pKa value was used such as $LiNO_3$; this is readily soluble in water [32].

In general, the support enhances the stabilization of the active species and promoters for the synthesis of higher alcohols; promotes the donation or exchange of hydrogen or oxygen; donates and receives electrons of metal particles; and controls the degree of reduction and dispersion [33]. Particularly in CO hydrogenation, strong interactions between supports and active metals have a significant influence on the synthesis of higher alcohols [34]. A strong metal-support interaction (SMSI) leads to changes of phase and morphology triggered by partial reduction of the active oxide or oxide supports. The formation of oxygen vacancy defects due to the reduction can cause strong bonding between the active metal and the surface of supports [35,36]. The shaping and sizing of active metals and supports can also exhibit strong SMSI due to their large surface-to-volume ratio [37]. In addition, doping small amounts of specific cations such as Li^+, Na^+, and Sr^{2+} to the catalyst affects the mutual solid-solid interactions between the components [38,39]. It indicates the necessity of a strong SMSIs catalyst, which provides a significant effect on the catalytic reaction.

Thus, we investigate the effect of alumina nanorods (ARs) as a support with a large surface-to-volume ratio on the activity of Cu-Zn-based catalysts promoted by Li and on the long-term thermal stability for effective conversion of syngas to higher alcohols.

2. Experimental section

2.1. Synthesis of γ-Al_2O_3 Nanorods

All chemicals were analytical grade reagents and were used as received without further purification. All experiments were conducted in air. The γ-Al_2O_3 nanorods as a support were synthesized using a boehmite precursor (see Supplementary Fig. S1 and S2) by a hydrothermal route [40]. A 1.00 M solution of aluminum chloride hexahydrate ($AlCl_3 \cdot 6H_2O$, Sigma Aldrich, 99%) was prepared with 100 ml distilled water under vigorous stirring at room temperature. Then, 1.00 M of 50 ml ammonia solution (28% NH_3 in water, Junsei) was added to 1.00 M of 50 ml sodium hydroxide (NaOH, Yukari, 96%) solution to prepare a mixed precipitant. The precipitant solution was added dropwise to the aluminum chloride solution, and the pH value was adjusted to 5 with ammonia solution. The mixture was transferred to a 330 ml Teflon-lined autoclave and kept at 200°C for 24 h. After the reaction, the resulting solution was centrifuged and washed three times with distilled water and ethanol then dried

at 80°C in a vacuum oven. The dried boehmite powder was calcinated in a box furnace and heated to 500°C (3°C/min) for 2 h in air.

2.2. Fabrication of Catalysts

For the catalyst preparation by co-precipitation (see Supplementary Fig. S3), solutions of nitrate and AR were prepared separately according to the molar ratio as shown in Table 1.

In order to investigate the effect of the introduction of ARs on Cu-Zn based catalysts, the catalysts containing with molar ratio of Cu:Zn = 5:5 and the amount of ARs was varied through co-precipitation as shown in Table 1 and Supplementary Table S1. The prepared ARs of 0−15 mol% were added to 125 ml of nitrate solutions according to the compositions of Table 1 and dispersed, and the catalysts were prepared by co-precipitation method. The nitrate precursors used were a 1.00 M solution of copper (II) nitrate trihydrate ($Cu(NO_3)_2{\cdot}3H_2O$, Junsei, 99%) and zinc nitrate hexahydrate ($Zn(NO_3)_2{\cdot}6H_2O$, Sigma Aldrich, 98%) (Cu:Zn = 5:5). 1.2 M Na_2CO_3 solution as a precipitant and the prepared solution added dropwise to hot distilled water (100 ml) at 65°C. During precipitation, the pH was kept at 6.5−7.5. After aging for 6 h, the precipitates were filtered and washed several times with distilled water and then dried at 80°C for 24 h in a vacuum oven. After grinding, the dried catalyst was calcinated at 350°C (3°C/min) under air for 4 h. The lithium promoter (0.5 wt%, Li) was doped to the resulting solids by vacuum impregnation with an aqueous solution of lithium nitrate ($LiNO_3$, Junsei, 98%) followed by drying and final calcination in air for 4 h at 350°C. To investigate the synergistic effect of the Al^{3+} ions and the ARs, the catalyst was prepared with a Cu:Zn ratio of 5:5 with 5−15 mol% of ARs, and the amount of Al^{3+} was varied through co-precipitation.

The catalysts were synthesized as described above except that the ratio of Cu:Zn:Al was changed with aluminum nitrate nonahydrate ($Al(NO_3)_3$, Junsei, 99%).

2.3 Catalyst characterization

The X-ray diffraction (XRD) patterns of the prepared catalysts were obtained using a diffractometer (M/S, Shimadzu Instruments, Japan) with Ni-filtered Cu Kα radiation at 40 kV and 30 mA. The Debye-Scherrer equation

was used to calculate the average metal particle size of all the catalysts.

Thermogravimetry/Differential Thermal Analysis (TG/DTA) was used to determine the thermal properties using an SDT Q 600 instrument (TA Instruments, USA). The samples were loaded into an alumina pan and heated to 900°C at a heating rate of 10°C/min with flowing air.

The BET surface areas of the Li-promoted catalysts were measured using an automated gas sorption system (Moon Sorp II, KIST); N_2 adsorption-desorption isotherms were obtained at 77 K. The pore diameters and volumes were calculated using the Barrett-Joyner-Halenda (BJH) method. The results are shown in Table 1.

The reduction characteristics were examined by temperature programmed reduction (TPR, AutoChem II 2920, Micromeritics, USA). The Li-promoted and calcined catalyst samples (100 mg) were placed between quartz wool in a U-type quartz reactor and pretreated under a flowing Ar stream at 300°C for 2 h to remove physically absorbed impurities and water, followed by cooling at room temperature under pure Ar gas. After pretreatment, the temperature was raised to 900°C at a heating rate of 10°C/min in a 5% H_2/He flow (30 ml/min).

X-ray photoelectron spectroscopy (XPS) was performed with a PHI 5000 Versa Probe (Ulvac-PHI) spectrometer using monochromated Al Kα (1486.6 eV) radiation. The binding energy was calibrated using the adventitious carbon peak at 284.6 eV. The background pressure in the analysis chamber was maintained in the 2.0×10^{-7} Pa range. Survey scans were recorded for surface elemental analysis (pass energy 117.4 eV), with high resolution spectra recorded at a pass energy of 46.95 eV.

Temperature Programmed Desorption (TPD) of CO_2 was performed with a Thermal Conductivity Detector (TCD)-TPD system (AutoChem II 2920, Micromeritics, USA). The Li-promoted and calcined catalyst samples (100 mg) were charged between quartz wool in a U-type quartz reactor, preheated under flowing He at 300°C for 2 h, and cooled to room temperature. After pretreatment, 10% CO_2/He as the absorption gas was passed at 60°C for 1 h and the samples were flushed with flowing He at 60°C for 1 h. The temperature was raised to 900°C at a heating rate of 10°C/min in a He flow. TCD was used to measure the amount of CO_2 absorbed on the catalysts.

To examine the morphology of the catalysts, scanning electron microscopy (SEM) imaging and energy dispersive analysis of X-rays (EDAX) studies were performed with an Inspect F50 instrument. For the SEM-EDAX measurements, samples were prepared on a carbon tape and coated with Pt.

2.4 Catalytic performance

Carbon monoxide hydrogenation to higher alcohols was measured in a stainless steel fixed-bed flow reactor (0.25 m height × 0.0102 m I.D., 0.0127 m O.D.) with 0.5 g catalysts. Prior to the reaction, the Li-promoted catalyst was reduced under pure H_2 at a flow rate of 30 ml/min at 300°C for 3 h. Then, the reactor was cooled to 493 K and the pressure of the reaction mixture was raised to 4.5 MPa. The reactions were carried out at 300°C. The molar ratio of the reactants (H_2/CO) was maintained at 1 throughout the studies and the space velocity (GHSV) at 4,000 ml Hg. The products were analyzed with an online gas chromatograph (HP -7890 A) with Porapak-Q and HP-Inno wax columns connected to a TCD and a Flame Ionization Detector (FID), respectively. The former column was used for the analysis of H_2, CO, CH_4, methanol, and CO_2, while the latter was used for the analysis of hydrocarbons and alcohols (C2–C5).

CO conversion was calculated as the mole percentage of carbon monoxide converted to products.

$$\text{CO conversion (mol\%)} = \frac{COin - COout}{COout} \times 100$$

The carbon selectivity was defined as the moles of carbon in a given product divided by the total moles of carbon converted in both the liquid and gas streams.

3. Results and discussion

3.1. Catalyst characterization

The crystalline phases were identified from the XRD patterns of as-prepared precursors and calcined catalysts shown in Fig. 1(A–D). Fig. 1(A) shows the change in the XRD patterns of the precursors according to the amount of ARs added to the catalysts. With added ARs, the aurichalcite phase and the malachite phase coexist, while only the aurichalcite phase exists in CZA(0)/0, which is defined in Table 1. Especially, the malachite phase is the best developed in CZA(0)/10. Fig. 1(B) shows XRD patterns of the catalysts with 10 mol% ARs and different amounts

of Al^{3+}. The CuZnAl hydrotalcite phase with a layered structure is formed in the catalysts with the addition of Al^{3+}, and the associated physicochemical properties are listed in Table 1. Three phases coexist in all the samples and the hydrotalcite phase is the most well-developed in CZA(12)/10 among other samples. Fig. 1(C) and (D) exhibit XRD patterns of catalysts that had calcined precursors and were finally calcined after Li promotion at 350°C. In the patterns, CuO appears at 2θ near 35° and Cu_2O near 36°. The crystallite sizes of CuO and Cu_2O decrease as the content of ARs added to the Li-promoted Cu-Zn catalysts in Fig. 1(C) increases. The sizes of CuO and Cu_2O further decrease as a result of addition of Al^{3+} to the Li-promoted Cu-Zn catalysts containing 10 mol% ARs, which results in an increased surface area. The increase in the specific surface area is related to the brucite-type hydrotalcite phase, in which Al^{3+} is partially substituted for anions (OH^- and CO_3^{2-}) in the interlayer [41] during formation and pyrolysis.

Fig. 2(A and B) and (C and D) show DTA and TG curves of the as-prepared precursors of the Cu-Zn catalyst and the Cu-Zn-Al catalyst, respectively. The endothermal peaks of the CZA(0)/0 catalyst appeared at around 242°C, corresponding to aurichalcite. For all the samples with added ARs (CZA(0)/5, 10, and 15), endothermal peaks appeared at around 375°C, corresponding to malachite. The results indicate that only aurichalcite exists in the catalyst CZA(0)/0, but aurichalcite and malachite coexist in the CZA(0) catalysts containing ARs [42]. In Fig. 2(B), the endothermal peaks at 139–153°C are assigned to the hydrotalcite due to the addition of Al^{3+}. Thermogravimetry (TG) curves in Fig. 2(C) and (D) show that the weight losses are assigned to the removal of structural water at 100–150°C [43], the first emission of CO_2 at around 370°C, and the second decarbonation at about 480°C.

Fig. 3(A) and (B) show the H_2 TPR profiles for the L-CZA(0) catalysts containing ARs and L-CZA containing 10 mol% ARs, respectively. In Fig. 3(A), L-CZA(0)/0 has peaks at 300°C with a broad shoulder at 389°C, but only one peak appeared for the L-CZA(0) catalysts containing ARs. The peaks at 260–300°C are assigned to the reduction of CuO and/or Cu_2O to Cu with H_2. The reduction temperature is shifted to a lower temperature as the content of ARs increases, which is due to the decrease in the crystallite size of CuO and Cu_2O as shown in Table 1. In particular, L-CZA (0)/0, which has a Cu_2O size of 8.99 nm, has a large shoulder peak. The addition of ARs not only reduces the crystallite size of CuO but also results in good dispersion [44]. Therefore, as the amount of added ARs increases, the reduction temperature shifts to a lower value, and L-CZA(0)/15 is reduced at 261°C,

which is approximately 40˚C lower than L-CZA(0)/0. The highly dispersed CuO is reduced at a much lower temperature than bulk CuO, which makes the catalyst active in the CO hydrogenation reaction in the synthesis of higher alcohols from syngas [26].

In Fig. 3(B), the TPR peaks shift from 281 to 300°C with the addition of Al^{3+} ions. Although the CuO crystallite size of L-CZA(0)/10 is nearly twice that of L-CZA(5)/10, the reduction peaks appeared at almost the same temperature, at 281 and 283°C, respectively. When the amount of Al^{3+} was increased to above 10 mol%, the peaks shifted significantly to higher temperatures, even though the crystallite size of CuO slightly increased compared to that of 5 mol% Al^{3+}. This means that refractory material can be formed in the catalysts containing Al^{3+}.

Fig. 4(A–D) shows the oxidation state of copper and the surface compositions of different catalysts determined with XPS. The Cu $2p_{3/2}$ core-level spectra of the four catalysts (L-CZA(0)/0, L-CZA(0)/10, L-CZA(10)/10, and L-CZA(12)/10) are displayed in Fig. 4, and the elemental analysis of the surface of the catalysts is shown in Table 2. From Fig. 4, it is clear that the catalysts display three components: a peak at around 932 eV assigned to Cu_2O [44], a peak at around 933 eV assigned to CuO, and a peak at about 935 eV assigned to a $CuAl_2O_4$ spinel type compound [3]. A satellite peak is also observed at about 943 eV, which is the fingerprint of Cu^{2+} ions. In the catalysts containing 10 mol% of ARs, listed in Table 2, the peak at around 935 eV is attributed to Cu^{2+} in $CuAl_2O_4$, and the peak at around 933 eV is assigned to Cu^{2+} in CuO. This indicates that amorphous $CuAl_2O_4$, which is invisible in the XRD patterns of Fig. 1(C) and (D), is formed due to the strong interaction between CuO and Al^{3+} ions, resulting in a greater shift in the reduction temperature at the TPR peaks in Fig. 3(B) despite the decrease in the CuO crystallite size.

Fig. 5 shows the effect of the phase change of the catalyst on the CuO crystallite size and the BET surface area at different AR contents. In Fig. 5(A), only the aurichalcite phase is observed in the catalyst without ARs, but the malachite phase is newly observed in the catalysts containing ARs. As the appearance of the malachite phase decreases the crystallite size of CuO from 11.42 to 6.34 nm, it increases the specific surface area from 20 to 38 m^2/g. As the content of ARs increases, the BET surface area, which is related to the CO conversion, also increases due to formation of the malachite phase. Fig. 5(B) shows the effect of the phase change incurred by addition of Al^{3+} to the catalysts, including the effect of the ARs on the CuO crystallite size and BET surface area. In the catalyst containing 5 mol% of Al^{3+}, the CuO size decreased by half and the BET surface area increased, which

was closely related to the formation of the hydrotalcite phase and its pyrolysis. The BET value increases with the Al^{3+} content at more than 5%, with a slight increase in the crystallite size of CuO. This is attributed to the formation of highly porous bodies by pyrolysis of the hydrotalcite phase, as shown in the XRD results in Fig. 1(B).

3.2. Catalytic performance in CO hydrogenation to higher alcohols

For the synthesis of higher alcohols, Li-promoted Cu-Zn catalysts with varying mol% of ARs and Al^{3+} were reacted at 300˚C and 4.5 MPa, and the conversion of CO and selectivity to the carbon-based products are shown in Table 3 and Fig. 6.

Fig. 6(A) and (B) show the selectivity to $C_{2+}OH$ according to the basicity at different contents of ARs and Al^{3+}. In Fig. 6(A), the selectivity to $C_{2+}OH$ increased with the basicity. Among the L-CZA catalysts with ARs, the selectivity was the highest at 8.7% with 15 mol% ARs. In Fig. 6(B), as the basicity increased with the addition of Al^{3+}, the $C_{2+}OH$ selectivity increased up to 10 mol% Al^{3+}, peaking at 17.55%, and then decreased at over 10 mol% Al^{3+}. The fact that the selectivity to $C_{2+}OH$ at 15 mol% decreases even though the basicity is 1.5 times higher than that at 10 mol% indicates that an optimal basicity is needed for maximum selectivity.

Fig. 6(C) and (D) show the CO conversion according to the BET surface area at different AR and Al^{3+} contents. In Fig. 6(C), the conversion of CO increased with the BET surface area, which is related to the decrease in the CuO crystallite size due to the addition of ARs. This indicates that the dispersion of Cu directly reacting with CO tends to be increased by reducing the size of CuO coated on the surface of the ARs [45]. The CO conversion was the highest at 12.77% at 15 mol% of ARs. In Fig. 6(D), the CO conversion was the highest at approximately 15% at 10 mol% Al^{3+} and then decreased to 12.6% at 12 mol% Al^{3+}. The CO conversion also increased with the BET surface area, which is related to the size of CuO formed by thermal decomposition of the hydrotalcite phase, except at 12 mol% Al^{3+}. The drop in the CO conversion at 12 mol% Al^{3+} is attributed to the increase in less-active amorphous $CuAl_2O_4$, as judged by the increase in the ratio of $CuAl_2O_4$/CuO shown in Table 2.

Fig. 7(A) and (B) show the distribution of alcohols in the reaction products obtained from L-CZA(0)/0, L-CZA(0)/10, L-CZA(10)/0, and L-CZA(10)/10 catalysts for a 6 h reaction. The 2-methyl branched alcohols such

as tert-pentyl alcohol and isopropyl alcohol were significantly increased and the primary product, methanol, was much decreased in the Li-promoted catalysts containing ARs, particularly ARs and Al^{3+}. It represents that the incorporation of nanorods and Al^{3+}, which lower the crystallite size of Cu and increase the basicity, play a crucial role in increasing the production of higher alcohols. Fig. 8 shows the morphologies of the catalysts before and after the reaction. Unlike the precursor of L-CZA(0)/0 without ARs, the precursors containing ARs are found to be rod-shaped, and the calcined and the reacted catalysts are also observed to have this shape. This is attributed to desintering by the formation of amorphous $CuAl_2O_4$ derived from the thermal decomposition of hydrotalcite precursors.

Fig. 9 shows the results of long-term stability tests on L-CZA(10)/0 and L-CZA(10)/10 at 300˚C for 40 h to investigate the effect of ARs on thermal stability. The conversions of H_2 and CO for 1 h and 40 h reactions are listed in Table 4. L-CZA(10)/10 containing ARs exhibits less catalytic deactivation and is more suitable for the long-term reaction than L-CZA(10)/0 without ARs. This demonstrates that the highly thermal resistant ARs helps prevent the catalyst from sintering and deactivating as the reaction proceeds. On the other hand, as shown in the XPS spectral results in Table 2 and Supplementary Table S2, the ratio of $CuAl_2O_4$/CuO in L-CZA(10)/10 is almost twice as large as that in L-CZA(10)/0 (see the detailed characteristics of L-CZA(10)/0 in Supplementary Fig. S4–S7, and Supplementary Table S1–S3), indicating that the thermally stable $CuAl_2O_4$ phase also improves the stability of the catalyst. Thus, it is found that the addition of ARs and the formation of $CuAl_2O_4$ prevent catalyst deactivation and enhance long-term catalytic stability.

The XRD patterns of the L-CZA(10)/0 and L-CZA(10)/10 catalysts with or without ARs after long-term stability tests are shown in Supplementary Fig. S8. Before the reaction, the reduction of CuO to Cu was performed, and this was sequentially reacted for 40 h. After reaction, Cu and ZnO phases were observed. The crystallite size of Cu in L-CZA(10)/10 was smaller than in L-CZA(10)/0, as shown in Table 5. Fig. 10 shows the TG-DSC curves of the reacted catalysts under air. The initial weight losses below 130˚C are caused by dehydration and the weight gains above 130˚C are due to oxidation of the catalysts in the order $Cu \rightarrow Cu_2O \rightarrow CuO$. Amorphous and graphite carbon were identified in TG-DSC, while the carbon species were not detected in the XRD patterns in Fig. 10. In Table 5, very low amounts of carbon below 2.0% were produced, indicating that neither catalyst is affected by coking. Therefore, it is found that the stability of the L-CZA(10)/10 catalyst is significantly improved by the

desintering of catalyst by the amorphous $CuAl_2O_4$ phase and nanorods, not by the coking resistance.

4. Conclusion

Addition of ARs and Al^{3+} ions to the Cu-Zn-based catalyst formed malachite and hydrotalcite phases in precursors that contained only the aurichalcite phase and affected the crystallite size and surface area. This phase change reduced the crystallite size of CuO and increased the BET surface area and basicity to improve CO conversion and $C_{2+}OH$ selectivity. In particular, L-CZA(10)/10 showed the highest catalytic activity with a CO conversion of 15% and a $C_{2+}OH$ selectivity of 17.5%, which was the most optimized for the synthesis of 2-methyl branched alcohols among the higher alcohol products. An appropriate ratio of $CuAl_2O_4$/CuO stabilizes the modified catalyst containing ARs and maintains the activity of the catalyst even when it is operated for 40 hours, which is attributed to desintering of the catalyst by the amorphous $CuAl_2O_4$ and nanorods.

Acknowledgments

We gratefully acknowledge financial support of this work from the Korea Institute of Science and Technology (Grant No. 2E27500).

References

[1] U.S. Department of Energy. Strategic Significance of America's Oil Shale Resource; Washington, DC, March 2004, http://www.fossil.energy. gov/programs/reserves/npr/publications/npr_strategic_significancev1.pdf.

[2] U.S. Energy Information Administration, U.S. Department of Energy. Annual Energy Outlook 2009; Washington, DC, March 2009, http://www.eia.doe.gov/oiaf/aeo/pdf/0383%282009%29.pdf

[3] J.J. Spivey, A. Egbebi, Chem. Soc. Rev., 36 (2007) 1514-1528.

[4] J. Wang, Y. Li, Y. Han, Y. Sun, Y. Fang, J. Zhao, Z. Qin, Chin. J. Catal., 30 (2009) 770-775.

[5] X. Ning, Z. An, J. He, J. Catal., 340 (2016) 236-247.

[6] V.R. Surisetty, A.K. Dalai, J. Kozinski, Appl. Catal., A, (2011).

[7] K. Kon, S.M.A. Hakim Siddiki, K.-i. Shimizu, J. Catal., 304 (2013) 63-71.

[8] S. Roy, G. Mpourmpakis, D.-Y. Hong, D.G. Vlachos, A. Bhan, R.J. Gorte, ACS Catal., 2 (2012) 1846-1853.

[9] V. Subramani, S.K. Gangwal, Energy Fuels, 22 (2008) 814-839.

[10] J. Hill, E. Nelson, D. Tilman, S. Polasky, D. Tiffany, Proc. Natl. Acad. Sci. U.S.A., 103 (2006) 11206-11210.

[11] V. Abdelsayed, D. Shekhawat, J.A. Poston, J.J. Spivey, Synthesis, Catal. Today, 207 (2013) 65-73.

[12] J. Li, P. Zhu, S. Zuo, Q. Huang, R. Zhou, Appl. Catal., A, 381 (2010) 261-266.

[13] X.-M. Wu, Y.-Y. Guo, J.-M. Zhou, G.-D. Lin, X. Dong, H.-B. Zhang, Appl. Catal., A, 340 (2008) 87-97.

[14] J.-J. Wang, J.-R. Xie, Y.-H. Huang, B.-H. Chen, G.-D. Lin, H.-B. Zhang, Appl. Catal., A, 468 (2013) 44-51.

[15] Y.Z. Fang, Y. Liu, L.H. Zhang, Appl. Catal., A, 397 (2011) 183-191.

[16] J. Slaa, J. Van Ommen, J. Ross, Catal. Today, 15 (1992) 129-148.

[17] K.J. Smith, R.B. Anderson, Can. J. Chem. Eng., 61 (1983) 40-45.

[18] L. Shi, W. Chu, S. Deng, J. Nat. Gas Chem., 20 (2011) 48-52.

[19] D. Mei, R. Rousseau, S.M. Kathmann, V.-A. Glezakou, M.H. Engelhard, W. Jiang, C. Wang, M.A. Gerber, J.F. White, D.J. Stevens, J. Catal., 271 (2010) 325-342.

[20] T.Y. Park, I.-S. Nam, Y.G. Kim, nd. Eng. Chem. Res., 36 (1997) 5246-5257.

[21] M. Xiang, D. Li, H. Xiao, J. Zhang, H. Qi, W. Li, B. Zhong, Y. Sun, Fuel, 87 (2008) 599-603.

[22] J. Dalmon, P. Chaumette, C. Mirodatos, Catal. Today, 15 (1992) 101-127.

[23] A.D. de Aquino, A.J.G. Cobo, Catal. Today, 65 (2001) 209-216.

[24] M. Jiang, G.-Z. Bian, Y.-L. Fu, J. Catal., 146 (1994) 144-154.

[25] M. Lin, K. Fang, D. Li, Y. Sun, Catal. Commun., 9 (2008) 1869-1873.

[26] E. Heracleous, E.T. Liakakou, A.A. Lappas, A.A. Lemonidou, Appl. Catal., A, 455 (2013) 145-154.

[27] J. Campos-Martín, J. Fierro, A. Guerrero-Ruiz, R. Herman, K. Klier, J. Catal., 163 (1996) 418-428.

[28] I. Boz, M. Sahibzada, I.S. Metcalfe, Ind. Eng. Chem. Res., 33 (1994) 2021-2028.

[29] K.J. Smith, R.B. Anderson, Can. J. Chem. Eng., 61 (1983) 40-45.

[30] G. Vedage, P. Himelfarb, G. Simmons, K. Klier, ACS Publications1985.

[31] N. Tienthao, M. Hassanzahediniaki, H. Alamdari, S. Kaliaguine, J. Catal., 245 (2007) 348-357.

[32] J.S. Lee, S. Kim, K.H. Lee, I.-S. Nam, J.S. Chung, Y.G. Kim, H.C. Woo, Appl. Catal., A, 110 (1994) 11-25.

[33] J. Hindermann, A. Deluzarche, R. Kieffer, A. Kiennemann, Can. J. Chem. Eng., 61 (1983) 20-28.

[34] J. Schumann, M. Eichelbaum, T. Lunkenbein, N. Thomas, M.C. Álvarez Galván, R. Schlögl, M. Behrens, ACS Catal., 5 (2015) 3260-3270.

[35] T.P. Braga, N. Essayem, A. Valentini, RSC Adv., 5 (2015) 93394-93402.

[36] R. Naumann d'Alnoncourt, M. Friedrich, E. Kunkes, D. Rosenthal, F. Girgsdies, B. Zhang, L. Shao, M. Schuster, M. Behrens, R. Schlögl, J. Catal., 317 (2014) 220-228.

[37] A. Nobile Jr., M. W., Davis JR., J. Catal., 116 (1989) 383-398.

[38] G. El-Shobaky, G. Fagal, A. Ghozza, M. Mokhtar, Colloids Surf., A, 142 (1998) 17-25.

[39] G. El-Shobaky, G. Fagal, M. Mokhtar, Appl. Catal., A, 155 (1997) 167-178.

[40] Q. Yang, Bull. Mater. Sci., 34 (2011) 239.

[41] C. Busetto, G. Del Piero, G. Manara, F. Trifiro, A. Vaccari, J. Catal., 85 (1984) 260-266.

[42] W. Fu, Z. Bao, W. Ding, K. Chou, Q. Li, Catal. Commun., 12 (2011) 505-509.

[43] R.L. Frost, Z. Ding, Acta, 405 (2003) 207-218.

[44] C. Zhu, A. Osherov, M.J. Panzer, Electrochim. Acta, 111 (2013) 771-778.

[45] R.T. Figueiredo, A. Martınez-Arias, M.L. Granados, J. Fierro, J. Catal., 178 (1998) 146-152.

List of Figure Captions

Fig. 1. XRD patterns of the Cu-Zn & Cu-Zn-Al catalysts: (A), (B) as-prepared catalyst (precursor); (C), (D) Li-promoted & calcinated catalyst.

Fig. 2. DTA profiles of precursors to (A) Cu-Zn catalysts; (B) Cu-Zn-Al catalysts. TG curves of precursors (C) Cu-Zn catalysts; (D) Cu-Zn-Al catalysts (A: aurichalcite, M: malachite, H: hydrotalcite).

Fig. 3. TPR patterns of Li-promoted (A) Cu-Zn catalysts with varying mol% of γ-Al_2O_3 nanorods; (B) Cu-Zn-Al catalysts with varying mol% of Al^{3+}.

Fig. 4. XPS spectra of (A) L-CZA(0)/0; (B) L-CZA(0)/10; (C) L-CZA(10)/10; (D) L-CZA(12)/10.

Fig. 5. Effect of crystalline phases on CuO crystallite size and BET surface area.

Fig. 6. (A), (B) effect of basicity, (C), (D) effect of BET surface area on catalytic performance (Reaction conditions: H_2/CO = 1; 4.5 MPa; 300°C, GHSV = 4000 h^{-1}; 6 h). (A) & (C) L-CZA(0)/0–15; (B) & (D) L-CZA(0–12)/10.

Fig. 7. Product distribution of alcohols over Li-promoted Cu-Zn & Cu-Zn-Al catalysts after 6 h reaction (Reaction conditions: H_2/CO = 1; 4.5 MPa; 300°C, GHSV = 4000 h^{-1}).

Fig. 8. SEM images of catalysts: the samples (A) as-prepared, (B) Li-doped, and (C) spent catalysts (Reaction conditions: H_2/CO = 1; 4.5 MPa; 300°C, GHSV = 4000 h^{-1}; 6 h).

Fig. 9. Long-term stability test of (A) L-CZA(10)/0; (B) L-CZA(10)/10 (Reaction conditions: H_2/CO = 1; 4.5 MPa; 300°C; GHSV = 4,000 h^{-1}; 40 h).

Fig. 10. TG-DSC of after long-term stability reaction. (A) L-CZA(10)/0; (B) L-CZA(10)/10.

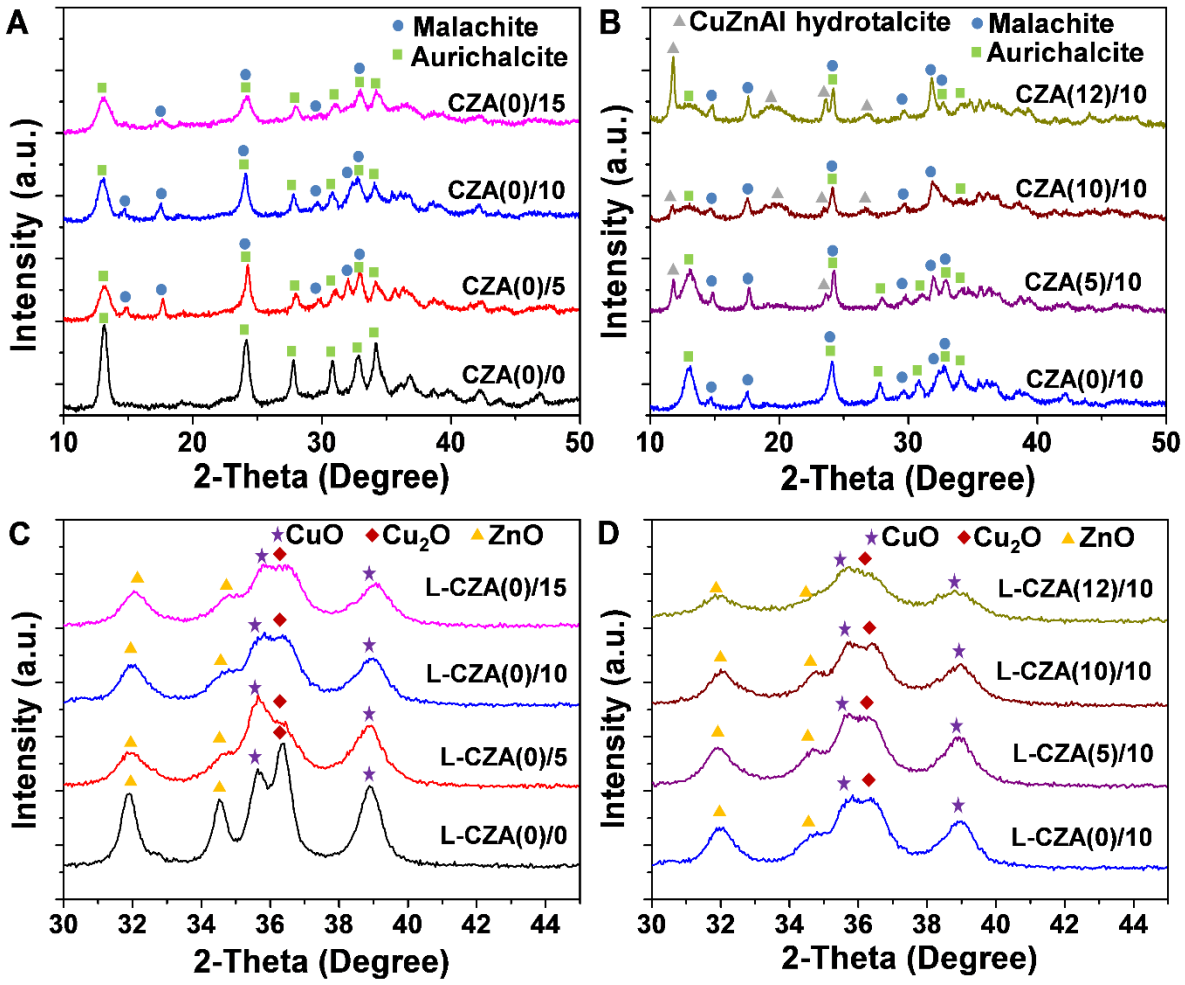

Fig. 1. S.M. Choi, et al.

Title: Effect of γ-Alumina Nanorods on CO Hydrogenation to Higher Alcohol over Lithium-Promoted CuZn-based Catalysts.

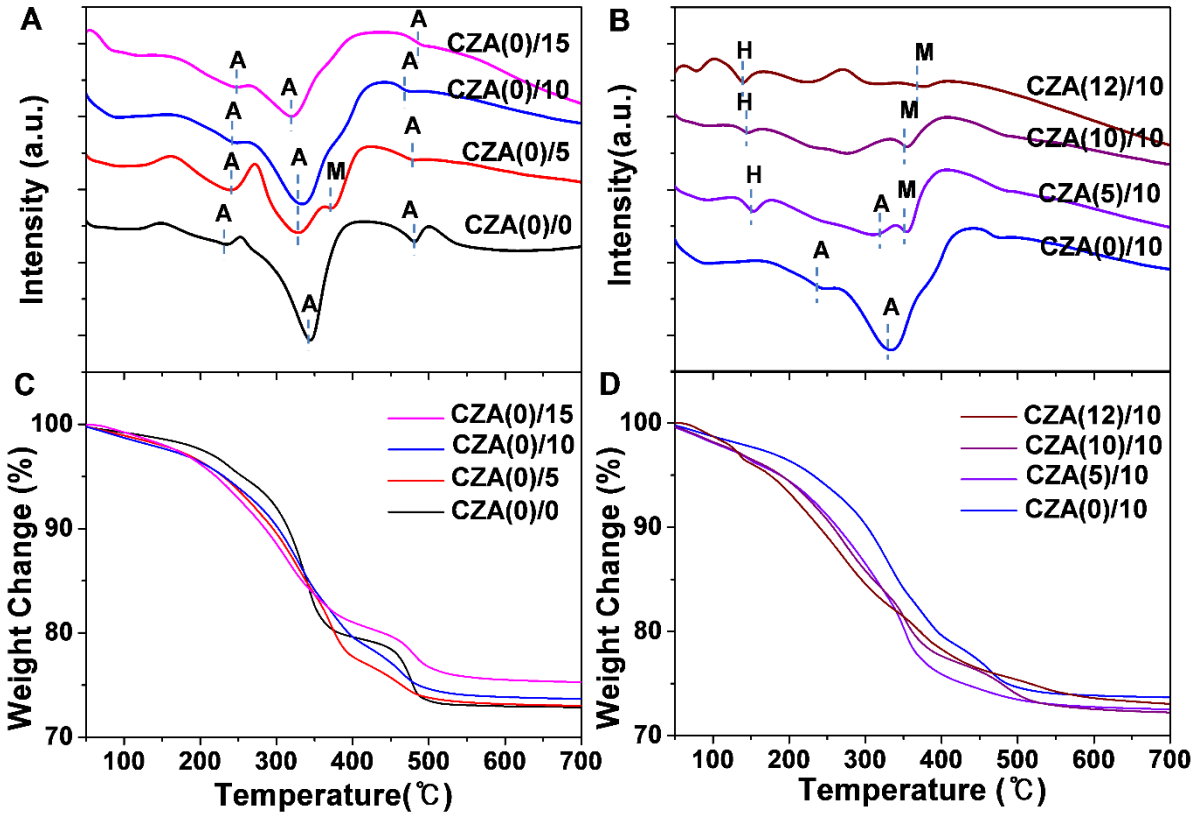

Fig. 2. S.M. Choi, et al.

Title: Effect of γ-Alumina Nanorods on CO Hydrogenation to Higher Alcohol over Lithium-Promoted CuZn-based Catalysts.

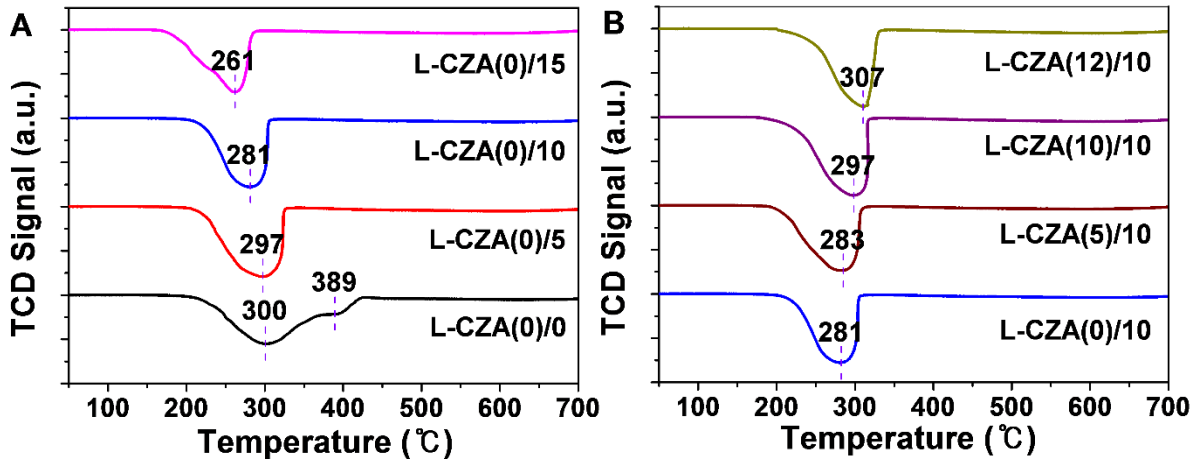

Fig. 3. S.M. Choi, et al.

Title: Effect of γ-Alumina Nanorods on CO Hydrogenation to Higher Alcohol over Lithium-Promoted CuZn-based Catalysts.

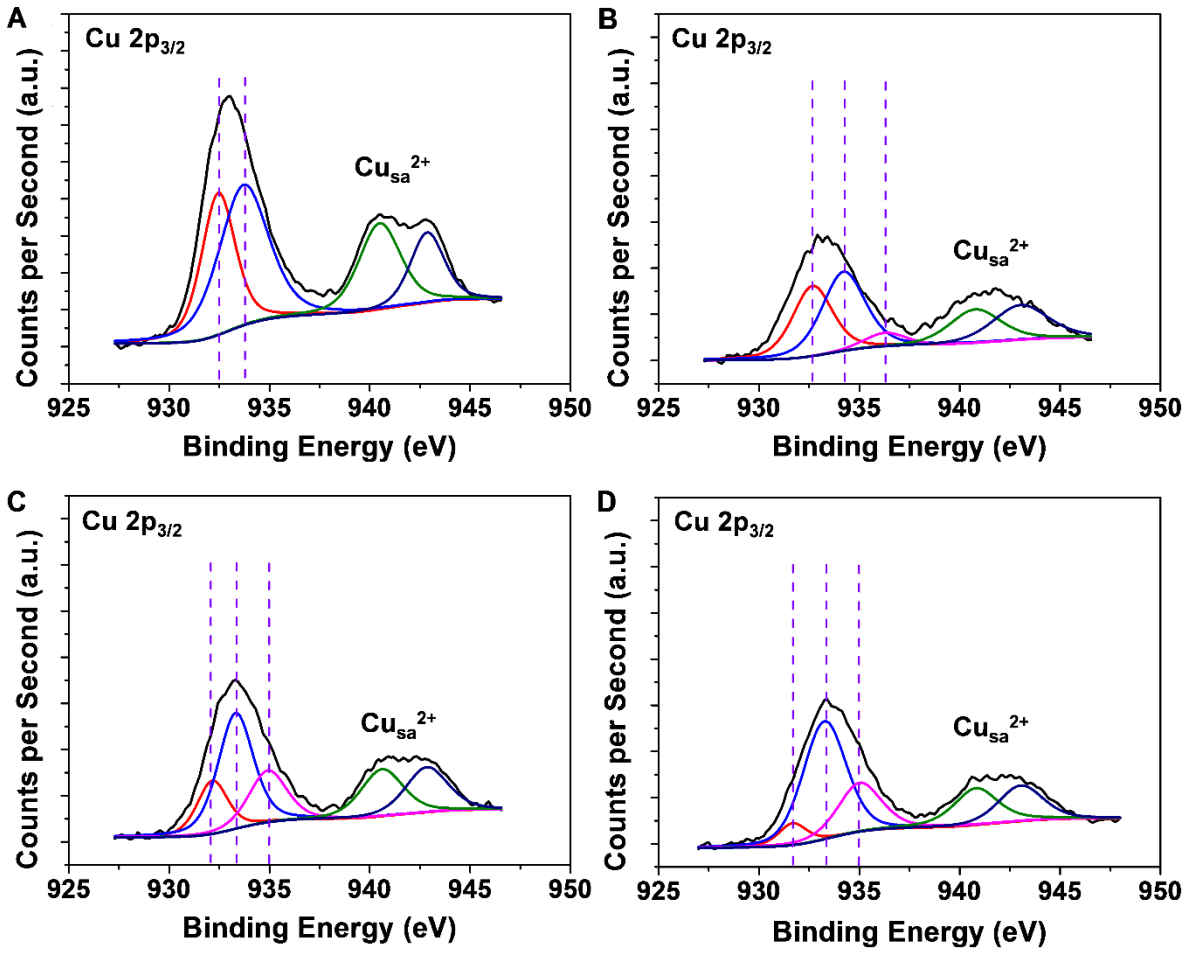

Fig. 4. S.M. Choi, et al.

Title: Effect of γ-Alumina Nanorods on CO Hydrogenation to Higher Alcohol over Lithium-Promoted CuZn-based Catalysts.

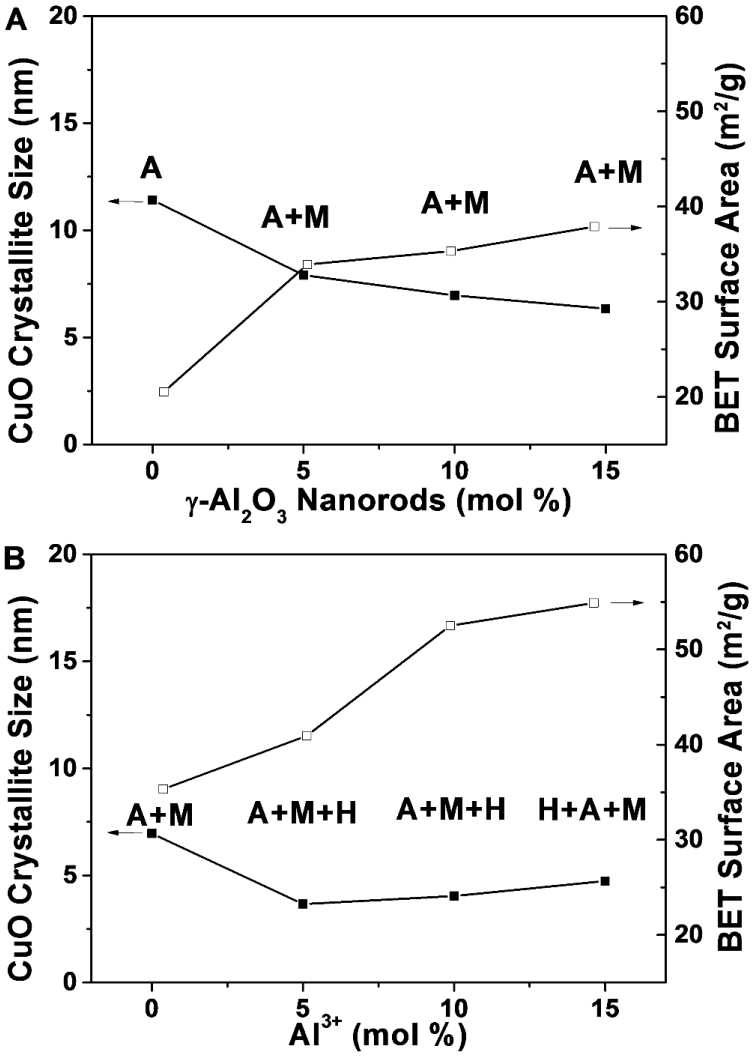

Fig. 5. S.M. Choi, et al.

Title: Effect of γ-Alumina Nanorods on CO Hydrogenation to Higher Alcohol over Lithium-Promoted CuZn-based Catalysts.

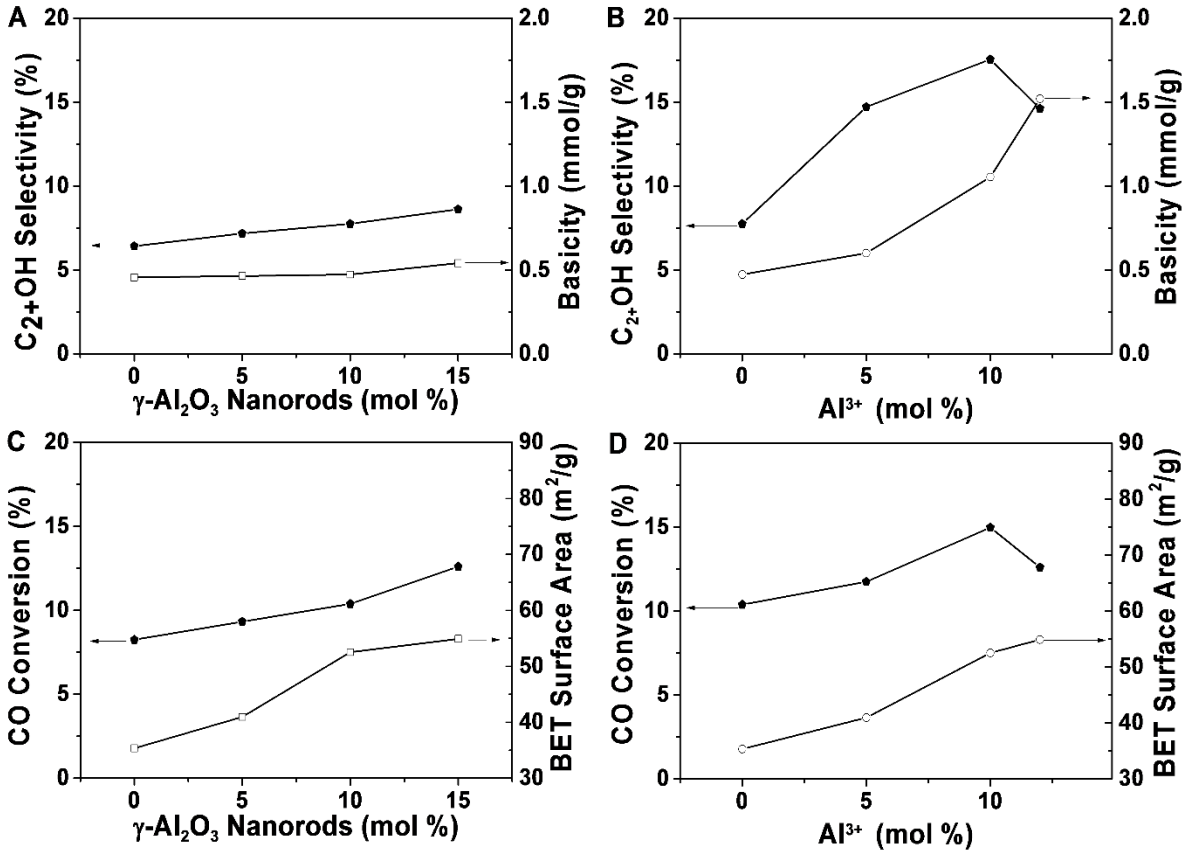

Fig. 6. S.M. Choi, et al.

Title: Effect of γ-Alumina Nanorods on CO Hydrogenation to Higher Alcohol over Lithium-Promoted CuZn-based Catalysts.

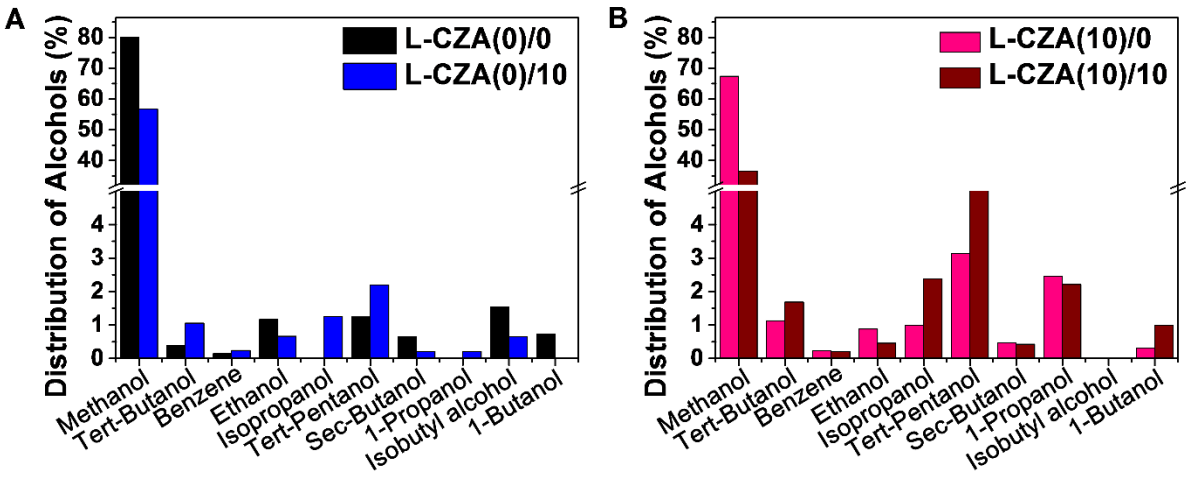

Fig. 7. S.M. Choi, et al.

Title: Effect of γ-Alumina Nanorods on CO Hydrogenation to Higher Alcohol over Lithium-Promoted CuZn-based Catalysts.

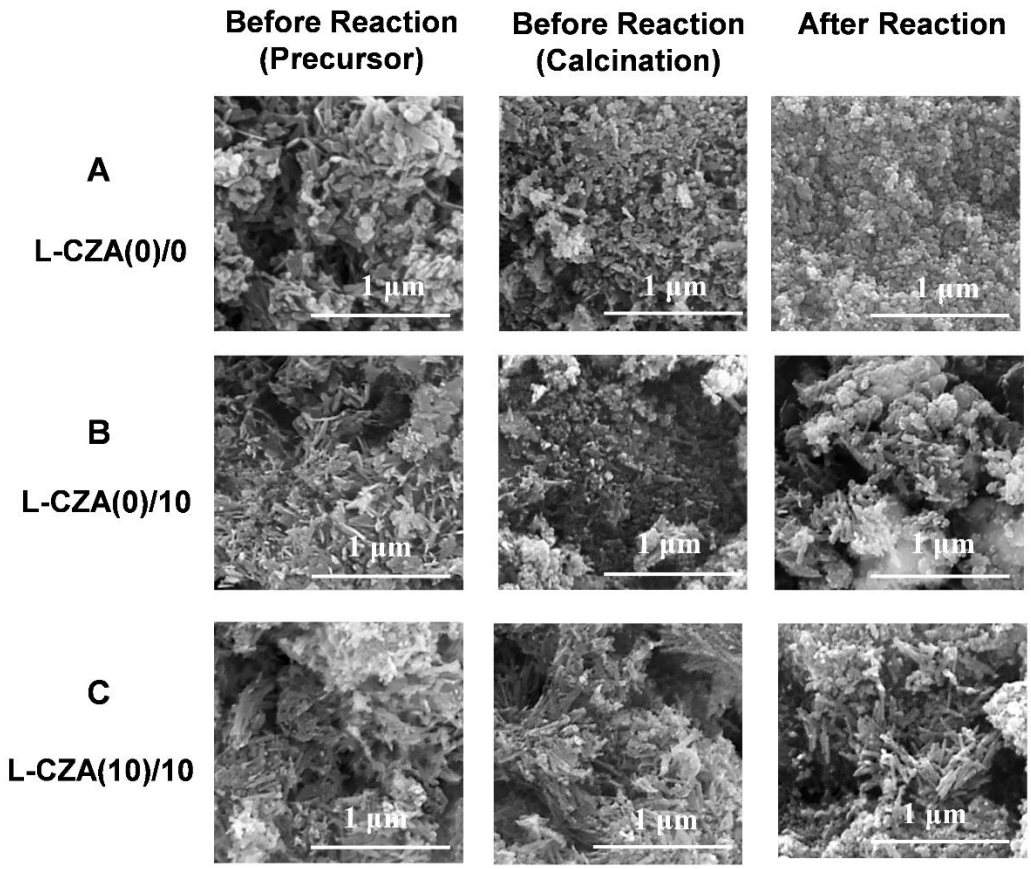

Fig. 8. S.M. Choi, et al.

Title: Effect of γ-Alumina Nanorods on CO Hydrogenation to Higher Alcohol over Lithium-Promoted CuZn-based Catalysts.

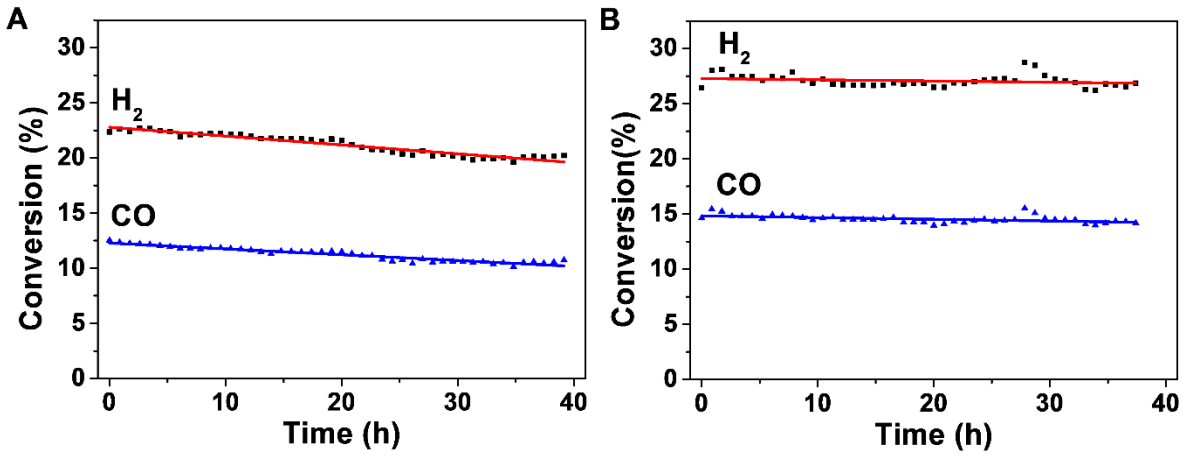

Fig. 9. S.M. Choi, et al.

Title: Effect of γ-Alumina Nanorods on CO Hydrogenation to Higher Alcohol over Lithium-Promoted CuZn-based Catalysts.

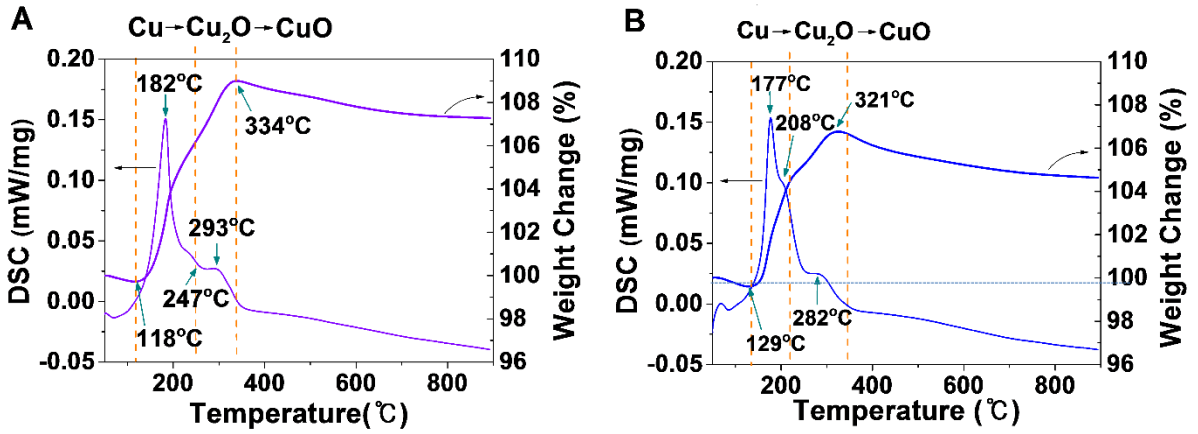

Fig. 10. S.M. Choi, et al.

Title: Effect of γ-Alumina Nanorods on CO Hydrogenation to Higher Alcohol over Lithium-Promoted CuZn-based Catalysts.

List of Table Captions

Table 1 Sample names, compositions of raw materials, and physicochemical properties of Li-promoted Cu-Zn-based catalysts.

Table 2 Binding energies of Cu $2p_{3/2}$ photoemission.

Table 3 Catalytic performance of Li-promoted Cu-Zn catalysts with varying mol% of ARs and Al^{3+}.

Table 4 The effect of ARs in Li-promoted Cu-Zn-Al catalysts on long-term stability test.

Table 5 Crystallite sizes of Cu and quantitative data of carbon deposited on the catalysts after long-term stability tests.

Table 1

Sample names, compositions of raw materials, and physicochemical properties of Li-promoted Cu-Zn-based catalysts.

Catalyst name	Li - Cu : Zn : Al		γ-Al_2O_3 nanorods/ (CuZnAl) (mol%)	**Phase	*BET Surface area (m^2/g)	*Pore Diameter (nm)	*Pore Volume (cc/g)	**Crystallite sizes (nm)		***Basicity (mmol/g)
	Li (wt%)	Cu:Zn:Al (mol%)						CuO	Cu_2O	
L-CZA(0)/0	0.5	50 : 50 : 0	0	**A**	20.54	40.12	0.20	11.42	8.99	0.45
L-CZA(0)/5	0.5	50 : 50 : 0	5	**A**+M	33.90	33.32	0.28	7.91	6.38	0.461
L-CZA(0)/10	0.5	50 : 50 : 0	10	**A**+M	35.32	36.57	0.32	6.96	6.12	0.47
L-CZA(0)/15	0.5	50 : 50 : 0	15	**A**+M	37.88	39.98	0.37	6.34	6.08	0.54
L-CZA(5)/10	0.5	47.5 : 47.5 : 5	10	**A+M**+H	40.92	42.08	0.28	3.66	6.81	0.60
L-CZA(10)/10	0.5	45 : 45 : 10	10	**A+M**+H	52.51	21.81	0.28	4.04	5.85	1.05
L-CZA(12)/10	0.5	44 : 44 : 12	10	**H**+A+M	54.87	26.19	0.35	4.74	3.72	1.52

*Textural properties were studied using low temperature (77 K) N_2-physisooprtion using Moonsorp-1.
**Phases were identified by XRD analysis. A: aurichalcite, M: malachite, and H: hydrotalcite.
***Basicity was measured by CO_2-TPD method.

Table 2

Binding energies of Cu $2p_{3/2}$ photoemission.

Catalyst name	BE Cu $2p_{3/2}$			Area ratio
	Cu^{+} (Cu_2O)	Cu^{2+} (CuO)	Cu^{2+} ($CuAl_2O_4$)	$CuAl_2O_4$/CuO
L-CZA(0)/0	932.45	933.71	-	-
L-CZA(0)/10	932.68	934.23	935.80	0.17
L-CZA(10)/10	932.15	933.31	934.92	0.48
L-CZA(12)/10	931.97	933.26	935.01	0.51

Table 3

Catalytic performance of Li-promoted Cu-Zn catalysts with varying mol% of ARs and Al^{3+}.

Catalyst name	CO conversion (%)	Carbon selectivity (Cmol%)		
		MeOH	$C_{2+}OH$	CO_2
L-CZA(0)/0	8.24	79.99	6.42	0.00
L-CZA(0)/5	9.32	64.48	7.18	2.51
L-CZA(0)/10	10.38	57.39	7.75	3.39
L-CZA(0)/15	12.77	64.68	8.14	4.61
L-CZA(5)/10	11.74	68.05	14.72	4.17
L-CZA(10)/10	14.97	36.60	17.55	7.72
L-CZA(12)/10	12.60	65.15	14.62	7.36

Reaction conditions: $H_2/CO = 1$; 4.5 MPa; 300℃; GHSV = 4000 h^{-1}, 6 h

Table 4

The effect of ARs in Li-promoted Cu-Zn-Al catalysts on long-term stability test.

Catalyst name	Conversion (%)			
	1 h		40 h	
	H_2	CO	H_2	CO
L-CZA(10)/0	22.6	12.52	20.07	10.45
L-CZA(10)/10	27.48	15.24	26.85	14.35

Reaction conditions: $H_2/CO = 1$; 4.5 MPa; 300℃; GHSV = 4000 h^{-1}.

Table 5
Crystallite sizes of Cu and quantitative data of carbon deposited on the catalysts after long-term stability tests.

Catalyst name	*Crystallite sizes (nm) Cu	**Amorphous Carbon (gC/gcat)[a]	**Graphite Carbon (gC/gcat)[b]	**Total amount of coke (%)
L-CZA(10)/0	12.33	0.7	0.9	1.6
L-CZA(10)/10	11.82	1.1	0.9	2.0

*Crystallite size was measured by XRD analysis.
**The amount of carbons were measured by TG analysis.
a: Amorphous carbon 300−400°C and b: Graphitic carbon > 500 °C.